The Journal of Chemical Physics

RESEARCH ARTICLE | JUNE 16 2023

All-electron APW+*lo* calculation of magnetic molecules with the SIRIUS domain-specific package

Long Zhang ; Anton Kozhevnikov ; Thomas Schulthess; S. B. Trickey ; Hai-Ping Cheng

J. Chem. Phys. 158, 234801 (2023)
https://doi.org/10.1063/5.0139497

The Journal of Chemical Physics ARTICLE scitation.org/journal/jcp

All-electron APW+*lo* calculation of magnetic molecules with the SIRIUS domain-specific package

Cite as: J. Chem. Phys. 158, 234801 (2023); doi: 10.1063/5.0139497
Submitted: 20 December 2022 • Accepted: 23 May 2023 •
Published Online: 16 June 2023

Long Zhang,[1,2,3,a] Anton Kozhevnikov,[4] Thomas Schulthess,[4] S. B. Trickey,[1,2,3] and Hai-Ping Cheng[1,2,3,b]

AFFILIATIONS

[1] Department of Physics, University of Florida, Gainesville, Florida 32611, USA
[2] Quantum Theory Project, University of Florida, Gainesville, Florida 32611, USA
[3] Center for Molecular Magnetic Quantum Materials, University of Florida, Gainesville, Florida 32611, USA
[4] Swiss National Supercomputing Centre, Lugano, Switzerland

[a] **Author to whom correspondence should be addressed:** longzhang2008@gmail.com
[b] **Electronic mail:** hping@ufl.edu

ABSTRACT

We report APW+*lo* (augmented plane wave plus local orbital) density functional theory (DFT) calculations of large molecular systems using the domain specific SIRIUS multi-functional DFT package. The APW and FLAPW (full potential linearized APW) task and data parallelism options and the advanced eigen-system solver provided by SIRIUS can be exploited for performance gains in ground state Kohn–Sham calculations on large systems. This approach is distinct from our prior use of SIRIUS as a library backend to another APW+*lo* or FLAPW code. We benchmark the code and demonstrate performance on several magnetic molecule and metal organic framework systems. We show that the SIRIUS package in itself is capable of handling systems as large as a several hundred atoms in the unit cell without having to make technical choices that result in the loss of accuracy with respect to that needed for the study of magnetic systems.

I. INTRODUCTION

Molecular magnetism, notably in the context of molecular magnetic materials, is a very active interdisciplinary research area that has significant implications for computational investigations. Motivated in no small measure by the promise of high impact on quantum computing,[1,2] molecular magnetism deals with the design, synthesis, and physical and chemical characterization of single-molecule magnets (SMMs),[3,4] spin-crossover molecules[5–8] and condensed aggregates thereof. Predictive and interpretive first-principles calculations are valuable both for experimental progress and for formulation and parametrization of models of the molecular spin systems. We begin therefore with a brief overview of the physical problem class and then turn to attendant computational challenges and some progress in meeting them.

A. Motivation from physical systems

Molecular magnetism involves a large range of dimensionality, from isolated SMMs[9,10] and 1D chain magnets[11,12] through 2D molecular layers[13] to 3D polymers and metal organic framework[14,15] materials that exhibit collective ordering of magnetic moments.

Growing research activity, both theoretical and experimental, has focused on (1) low dimensional materials (motivated by their potential application in high-density magnetic storage and nano-scale devices)[16,17] and (2) the so-called functional materials[9,16,18,19] (because of their strong response to changing external conditions). Because molecular magnets have well-localized magnetic moments, they provide a nearly perfect arena for investigation of intriguing phenomena and testing models. Distinct from bulk magnetic materials, their quantum size effects suggest applications beyond conventional high-density information storage. Example applications include spintronics and qubits for quantum computing.

The molecules involved are large and rather complicated. An example category is Mn_{12} complexes.[20] Their investigation dates to synthesis by Weinland and Fischer in 1921,[21] yet the crystal structure was not determined until 1980.[22] That particular Mn_{12} molecule is built from four Mn_{4+} ($S = 3/2$) and eight Mn_{3+} ($S = 2$) ions

coupled by oxygen atoms. The $[Mn_{12}O_{12}(O_2CPh)_{16}(H_2O)_4]$ complex was studied beginning in 1988,[23] and its ground state eventually determined[24,25] to have $S = 10$. For computational context, note that this system has 176 atoms and 1210 electrons.

A major class of experimental effort has focused on the design and synthesis of multi-nuclear clusters containing[4] Mn^{3+} because the axially Jahn–Teller (JT) distorted Mn^{3+} ionic positions usually cause large magnetic anisotropy due to spin–orbit coupling. A large number of Mn(III)-based SMMs has been reported, including those with Mn_6,[26] Mn_{19},[27–29] Mn_{25},[30,31] Mn_{31},[32] and Mn_{84}.[33] In addition, many transition metal (TM) SMMs based upon anisotropic V^{3+}, $Fe^{2+/3+}$, Ni^{2+}, and Co^{2+} ions have been synthesized; see Refs. 3 and 34–39. The octa-nuclear cluster $[Fe_8O_2(OH)_{12}][(tacn)_6]^{8+}$ (Fe^8), where (tacn) is the organic compound $C_6H_{12}(NH)_3$, reported by Sangregorio *et al.*[35] is an example. It has 174 atoms and 756 electrons with a $S = 10$ ground state that arises from competing anti-ferromagnetic interactions among eight Fe^{3+} ($S = 5/2$) ions.[40] Magnetic measurements revealed that it has an anisotropy energy barrier of 17 cm^{-1} induced by magnetic anisotropy. This is much smaller than that of the Mn_{12} complexes. Other significant synthesis effort has been focused on enhancing the magnetic anisotropy of the molecule.[41–44] That has stimulated the development of several different groups of SMMs, including cyano-bridged SMMs,[45–47] Ln-based SMMs,[48–52] 3*d*-4*f*-element-based SMMs,[50,53] actinide-based SMMs,[51] radical-bridged SMMs,[54] and organo-metallic SMMs.[55]

The critical setting regarding insightful computational studies provided by this brief overview is straightforward. SMMs are large, structurally and electronically intricate molecules with complicated spin manifolds. Materials comprised of them are, of necessity, more complicated and demanding. Many of the chemical details of SMMs are largely irrelevant to that assessment. However, the presence of heavy nuclei and the importance of anisotropy both suggest the significance of relativistic effects, including spin–orbit coupling (SOC). Predictive, materials-specific simulations of systems composed from SMMs thus are extremely challenging. Spin crossover (SCO) systems pose quite similar challenges.

B. Predictive computational approaches

The all-electron full-potential linearized augmented plane wave (FLAPW) basis is one well-tested form for implementation of the Kohn–Sham (KS) formalism[56,57] of the density functional theory (DFT).[58] A related form is APW+*lo*, augmented plane waves plus local orbitals. This family of basis sets is based on a partitioning of the unit cell of a material into non-overlapping muffin-tin (MT) spheres, centered at the atomic nuclei, and an interstitial (IS) region between the MT spheres, as illustrated in Fig. 1.

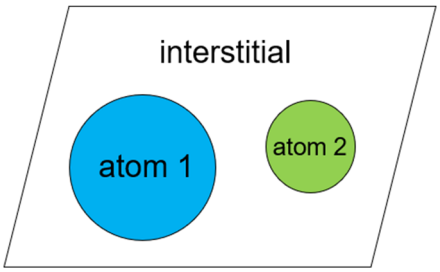

FIG. 1. The muffin-tin partitioning of a unit cell in (L)APW+*lo*, where the total volume of the unit cell is divided into the interstitial region and the muffin-tin spheres (color circles) centered at the positions of the atoms.

These basis sets originated from the APW method proposed by Slater.[59,60] It involved a non-linear eigenvalue problem for the determination of the MT basis functions themselves. A significant step forward was the introduction of linearized methods by Andersen[61] and applied by Koelling and Arbman[62] using the muffin-tin approximation to the potential. They also pointed out that the FLAPW made non-muffin-tin calculations feasible. The basis set is constructed according to the same space partition. One piece of the basis function for the Bloch wave-vector $\boldsymbol{k}$ and plane-wave vector $\boldsymbol{G}$ is

$$\varphi_{\boldsymbol{k}}^{\boldsymbol{G}}(\boldsymbol{r}) = \begin{cases} \sum_{\ell,m}\sum_{v} A_{\ell m v}^{\alpha,\boldsymbol{k}}(\boldsymbol{G})\, u_{\ell v}^{\alpha}(r) Y_{\ell m}(\hat{\boldsymbol{r}}), & \boldsymbol{r} \in \alpha, \\ (1/\sqrt{\Omega}) e^{i(\boldsymbol{G}+\boldsymbol{k})\cdot\boldsymbol{r}}, & \boldsymbol{r} \notin \alpha. \end{cases} \tag{1}$$

Here, $u_{lv}^{\alpha}(r)$ is the solution of the (energy dependent) radial Schrödinger equation in the MT sphere labeled α, $Y_{\ell m}(\hat{\boldsymbol{r}})$ are spherical harmonics, $A_{\ell m v}^{\alpha,\boldsymbol{k}}(\boldsymbol{G})$ are the matching coefficients for connection with the interstitial plane wave, ℓ and m are the azimuthal and magnetic quantum numbers in a particular sphere, and v is the order of energy derivative of the radial function. The APW basis set does not have continuous radial first derivatives at the sphere boundaries. The dependence of the radial functions upon the energy for which they are solved is the APW basis difficulty. Continuity at sphere boundaries requires those energies to correspond to KS eigenvalues. That correspondence makes the KS secular equation highly non-linear in the one-electron energies. The problem is remedied by introducing the energy derivative of the radial function to the basis, $\dot{u}_{\ell v}^{\alpha} = [\partial/\partial\varepsilon] u_{\ell v}^{\alpha}$. The resulting linearized APW (LAPW) basis is ordinary, in the sense of being decoupled from explicit dependence on the KS eigenvalues. The basis can be enhanced by addition of local orbitals (lo), which are radial functions and energy derivatives that vanish at the MT boundaries.

For any of these APW-based forms, the electron density and the effective potential are expanded in correspondence to the space division in the unit cell. In the interstitial region, they are expanded in plane waves, while inside the MT spheres, the expansion is in real spherical harmonics $R_{\ell m}(\boldsymbol{r})$,

$$n(\boldsymbol{r}) = \begin{cases} \sum_{\ell m} n_{\ell m}^{\alpha}(r) R_{\ell m}(\hat{\boldsymbol{r}}), & \boldsymbol{r} \in \alpha, \\ \sum_{\boldsymbol{G}} \tilde{n}(\boldsymbol{G}) e^{i\boldsymbol{G}\cdot\boldsymbol{r}}, & \boldsymbol{r} \notin \alpha \end{cases} \tag{2}$$

and

$$v_{KS}(\boldsymbol{r}) = \begin{cases} \sum_{\ell m} v_{\ell m}^{\alpha}(r) R_{\ell m}(\hat{\boldsymbol{r}}), & \boldsymbol{r} \in \alpha, \\ \sum_{\boldsymbol{G}} \tilde{v}(\boldsymbol{G}) e^{i\boldsymbol{G}\cdot\boldsymbol{r}}, & \boldsymbol{r} \notin \alpha. \end{cases} \tag{3}$$

Here, $n_{\ell m}^{\alpha}(r)$, $\tilde{n}(\boldsymbol{G})$, $v_{\ell m}^{\alpha}(r)$, and $\tilde{v}(\boldsymbol{G})$ are expansion coefficients determined through the self-consistent solution of the KS equation.

Since the KS equation that is solved has no reliance on pseudopotentials (PP) or projector augmented waves (PAW), the FLAPW and APW+*lo* solutions are commonly considered and used as a

highly precise ("gold standard") realization of DFT against which the precision of other computational implementations of DFT is tested. The trade-off is that the full-potential all-electron approach generally require more computational resources than PP and PAW methods, and addressing the computational efficiency motivates the focus of the present work upon the domain-specific SIRIUS package. Our goal here is to exploit SIRIUS to make fast and efficient all-electron, full-potential DFT calculations routinely feasible for large and complicated systems as exemplified by magnetic molecules and their aggregates. In Secs. II–VI, first we describe the package and its intended usage for accelerating plane-wave based DFT codes. We then explain its value when used as a stand-alone FLAPW/APW+*lo* package. Then, we demonstrate its capabilities by calculations on a selection of magnetic molecules.

II. THE SIRIUS PACKAGE

Irrespective of the particular code, FLAPW/APW+*lo* calculations obviously have the same underlying formalism. Because those basis sets start from plane waves, such codes also have significant elements in common with plane-wave pseudo-potential (PW-PP) codes. Those elements include the following: unit cell setup, atomic configurations, definition and generation of reciprocal lattice vectors $\boldsymbol{G}$ and combinations with Bloch wave vectors $\boldsymbol{G}+\boldsymbol{k}$, and definition of basis functions on regular grids as Fourier expansion coefficients; construction of the plane-wave contributions to the KS Hamiltonian matrix and generation of the charge density, effective potential, and magnetization on a regular grid; symmetrization operations on the charge density, potential, and occupation matrix; iteration-to-iteration mixing schemes for density and potential; and diagonalization of the secular equation. As already is evident, compared to PW-PP codes, FLAPW/APW+*lo* codes also have everything expanded in radial functions and spherical harmonics inside the MT spheres, along with the enforcement of matching conditions on sphere surfaces.

As we have discussed elsewhere,[63] those commonalities offer an opportunity, namely, *separation of concerns*. For those generally common tasks in FLAPW/APW+*lo* and PW-PP codes, the concept is to create a performance-optimized package with enough user support that it can be exploited either as a basic code or as a library. This strategy allows the abstraction and encapsulation of the common objects just listed, thereby exposing opportunities for optimizing computational performance irrespective of the user interface (input, post-processing, etc). The SIRIUS package was designed from the outset and developed from the outset with that goal. It provides both task and data parallelization. It is optimized for message passing interface (MPI) levels as well as OpenMP parallelization and for graphics processing unit (GPU) utilization as well.

SIRIUS can be interfaced directly with both existing FLAPW/APW+*lo* codes and with PW-PP codes as a *DFT library*. We have presented an example of such use elsewhere.[63] Although that was the original intention for the primary usage of SIRIUS, it turns out to have some limitations imposed by design incompatibilities structured into the host code. However, SIRIUS does have basic FLAPW/LAPW+*lo* stand-alone capability. Thus, there is opportunity to see what benefits can be gained for large-scale magnetic system calculations in that mode of SIRIUS usage, which is the topic of the current work. Additional implementation details of SIRIUS and the treatment of magnetism and spin–orbit coupling can be found in Appendixes A and B.

Motivated by the demands of large-system calculations, SIRIUS is designed and implemented with both task distribution and data (large array) distribution in mind. Note that typical KS calculations in a basis set rely on two basic functionalities: distributed complex matrix-matrix multiplication (`pzgemm` in LAPACK[64]) and a distributed generalized eigenvalue solver (`pzhegvx` also in LAPACK). SIRIUS handles these two major tasks with data distribution and multiple levels of task distribution. For computational capability, switching from LAPACK to ScaLAPACK gives the benefit of data parallelism but does not remove the diagonalization algorithm limitation. Switching from LAPACK (or ScaLAPACK) to a Davidson-type diagonalization addresses that. Doing so requires taking into consideration both the diagonalization algorithm and the handling of large datasets as the system size grows. This is especially so in the case of iterative diagonalization implemented in FLAPW/LAPW+*lo* basis codes. When the unit cell is as large as 10 Å^3 and contains a 100 or more multi-electron atoms, the plane-wave cutoff needed is normally about 25–30 a_0^{-1} (where a_0 is the Bohr radius) to reach a properly converged ground state. This causes the reciprocal-lattice-vector (G-vector) related arrays to become very large.

The problem is illustrated by the ELK and *exciting* codes. Each has several multi-dimensional arrays that have one dimension for the global G-vector indices. Because those arrays are not handled in a distributed way, they become very memory consuming in a single MPI task. Eventually, they become the real bottleneck once the diagonalization algorithm limitation is removed via a Davidson-type method. SIRIUS, in contrast, treats the G-vector related multi-dimensional arrays in a distributed manner by design.

As noted already, standard libraries do not offer Davidson-type diagonalization algorithms because they utilize repeated application of the Hamiltonian to a sub-space of the system. Algorithmic implementation therefore depends on the construction details of the Hamiltonian matrix, i.e., it depends on the specific DFT formalism. Again, the SIRUS package takes this into consideration by design. It provides an efficient implementation of Davidson-type diagonalization[65] for both FLAPW/APW+*lo* and PW-PP codes.

With the foregoing discussion for context, we turn to examples of stand-alone SIRIUS calculations on large molecular magnetic and spin crossover systems that exemplify our interest.

III. SIRIUS: [Mn(taa)] MOLECULE

Because it has proven to be a difficult case,[8] the first system studied is a molecular spin crossover (SCO) complex called [Mn(taa)]. Such systems often are found in transition metal compounds and metal organic frameworks. The SCO transition can be induced by a variety of external perturbations, e.g., as temperature, pressure, magnetic, and electric field. SCO molecular materials have potential utility for reversible molecular switching in functional materials. The [Mn(taa)] molecule ($[Mn^{3+}(pyrol)_3(tren)]$) is a meridional pseudo-octahedral chelate complex of a single Mn ion as the magnetic center and the hexadentate tris[(E)-1-(2-azolyl)-2-azabut-1-en-4-yl]amine ligand, as shown in Fig. 2 It has 53 atoms and 224 electrons.

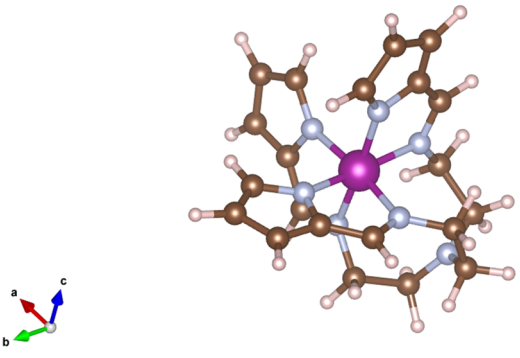

FIG. 2. The [Mn(taa)] molecule contains 1 Mn-atom (purple), 7 N-atoms (light blue), 21 C-atoms (brown), and 24 H-atoms (light brown).

Originally studied by Sim and Sinn,[66] it was the first known example of a Mn(III) $3d^4$ SCO system. Experimentally, it is an example of a transition that can be induced by application of an external magnetic field. Without any external magnetic field, the Mn^{3+} cation goes from a low-spin (LS) state (S = 1) to a high-spin (HS) state of (S = 2) at a transition temperature of about 45 K. The total energy difference between LS and HS states, $\Delta E_{HL} = E^{tot}_{HS} - E^{tot}_{LS}$, is relatively small, which makes magnetic-field-induced SCO transition experimentally feasible. Since the SCO is caused by the change of $3d$ electron configuration, the transition to the HS state is accompanied with not only a variation of dielectric constant but also an enhancement of the lattice volume. An important feature of the SCO transition of [Mn(taa)] is that the reorientation of the electric dipole moments appears to arise from the dynamic Jahn–Teller (JT) effect in the HS state.[67] Detailed first-principles calculation in combination with Monte Carlo simulation disclosed three competing HS phases: a Jahn–Teller ordered (solid) phase, a dynamically correlated (liquid) phase, and an uncorrelated (gas) phase.[68] The system poses challenges to the computational determination of the ground state due to the aforementioned small scale of ΔE_{HL} relative to the total energy magnitudes. Estimates are about 50 ± 30 meV but as high as a few hundred meV depending upon the exchange–correlation (XC) approximation used and various technical details.[8] Note that usual XC approximations suffer from a self-interaction error and, hence, tend to favor the LS state to reduce spurious self-repulsion with the result of overestimated ΔE_{HL} values. That is not our concern in the current work since what we are testing is the capability of SIRIUS in finding the LS ground state.

Several factors can affect a DFT calculation of the molecular ground state significantly. For consistency with condensed phase calculations, it is appropriate to study the isolated molecule in a large, periodically bounded box. To attain required accuracy, the plane wave cutoff needs to be large. For the isolated molecule, the vacuum volume in the computational unit cell requires even larger cutoffs. This makes the APW+*lo* calculation an intensive job because of the comparatively large Hamiltonian matrix to be diagonalized and the large *G*-vector related arrays.

The quality of APW+*lo* calculations is governed by the dimensionless quantity $R^{MT}_{\min} \cdot |\boldsymbol{G}^k|_{\max}$, where $R^{MT}_{\min}$ is the minimum muffin-tin radius of all atomic species and $|\boldsymbol{G}^k|_{\max}$ is the maximum $\boldsymbol{G} + \boldsymbol{k}$ vector magnitude. A common default value of $R^{MT}_{\min} \cdot |\boldsymbol{G}^k|_{\max}$ is 7 in most FLAPW/APW+*lo* codes. It can be 10 if one wants to push the accuracy of total energy to be close to μHa. For organic molecules, the smallest R^{MT} is normally around $1.4a_0$ for an H atom, which puts $|\boldsymbol{G}^k|_{\max} \in [5, 7]\, a_0^{-1}$. The size of the Hamiltonian matrix in the first variational step is determined by $|\boldsymbol{G}^k|_{\max}$, the total number of atoms, and the local orbitals added to each atom.

TABLE I. Input parameters for the [Mn(taa)] LS state.

Structure	Mn-taa, LS state structure
Unit cell	20 × 20 × 20 Å^3 box
Number of atoms	53
R_{mt} (a_0)	Mn: 2.2; O: 1.6; C: 1.4; H: 1.0;
$R^{MT}_{\min} \cdot \lvert\boldsymbol{G}^k\rvert_{\max}$	5
$\lvert\boldsymbol{G}_{\max}\rvert$ (a_0^{-1}) for ρ and V_{eff}	30
$l_{\max}$ for APW	8
$l_{\max}$ for ρ and V_{eff}	8
Size of basis set	≈165 000
k-point grid	1 × 1 × 1
(L)APW configuration	$\varepsilon_l = -0.15$ eV; $\partial_E = 0$;
lo configuration	Mn: s, p, d; O/C: s, p; H: s;
Treated as core state	Mn: 1s, 2s, 2p, 3s; O/C: 1s
Total energy tolerance	10^{-6} hartree
Potential tolerance	10^{-7} hartree
Run job setup:	16 MPI tasks 16 OMP threads per task
Number of SCF iterations	75 (VASP: 62)
Average time per SCF iteration	55 s
HOMO-LUMO gap (eV)	0.68 (VASP: 0.66)
μ_{tot} (μ_B)	Total: 2.00 (VASP: 2.00) Mn atom: 1.68 (VASP: 1.77)

For [Mn(taa)], if one sets $R^{MT}_{\min} \cdot |\boldsymbol{G}^k|_{\max} = 7$ and other parameters as shown in Table I, the dimension of the first variational Hamiltonian matrix is about 330 000. This is actually within the theoretical limit of the full diagonalization algorithm in LAPACK. However, in order to run the DFT calculation, not only the $\boldsymbol{G}^k$ vectors but also the $\boldsymbol{G}$ vectors for expanding density and potential must be handled efficiently. For molecules in a large cubic unit cell of the size of 20 Å with irregular vacuum space, we found (from SIRIUS calculations) that the $|\boldsymbol{G}|$ for density and potential needs to be as large as $25–30\, a_0^{-1}$ to make the total energy converge. If the arrays containing $\boldsymbol{G}$ vector indices are not stored in a distributed way, they become the major memory consuming quantities, which makes the calculation very slow.

The difficulty is real. We have tried to use community codes, such as ELK and Exciting-Plus, to calculate the ground state of [Mn(taa)] and found it to be quite difficult. If one performs a single k-point calculation for an isolated system, the lack of band parallelism within a k-point makes the run have only one MPI task. As just noted, the large $|\boldsymbol{G}|$ cutoff needed for density and potential implicates significant memory allocation that makes the calculation slow. A test to run the [Mn(taa)] system using Exciting-Plus on the NERSC Cori system (128 GB memory per node) with $|\boldsymbol{G}| = 30\, a_0^{-1}$ or larger caused a crash out-of-memory (OOM) error, even if one

TABLE II. Peak memory consumption of single *k*-point [Mn(taa)] calculation in a cubic unit cell of 20 Å. Other input parameters were the same as Table I.

$\|\boldsymbol{G}\|_{\max}$ (a_0^{-1})	20	25	30	35
Peak memory (GB)	39.5	110.8	151.8	209.5

node was assigned with only one MPI task. To have a more specific measure of the memory issue, we ran the same test, using Exciting-Plus, on the University of Florida HiperGator HPC large memory node and observed the peak memory consumption values reported in Table II.

For the SIRIUS calculation of [Mn(taa)], we used the experimentally determined low spin structures and the Perdew–Burke–Ernzerhof (PBE)[69] generalized gradient approximation (GGA) XC functional. We set $R_{\min}^{MT} \cdot |\boldsymbol{G}^k|_{\max} = 5$, $|\boldsymbol{G}|_{\max} = 30\, a_0^{-1}$, and other input parameter values listed in Table I. There was no Hubbard U. The same structures and XC were used in a Vienna *Ab initio* Simulation Package (VASP)[70] calculation for comparing the results; see Table I.

The ground state HOMO-LUMO gap from SIRIUS is 3% larger than that from the VASP calculation. The difference is small so that it does not suggest significant difference in physical or chemical properties. The total magnetization for the two calculations agrees at 2.00 μ_B. The Mn atom moments are 1.68 and 1.77 μ_B from SIRIUS and VASP, respectively. The difference arises from the fact that the muffin-tin radius for Mn in SIRIUS is 2.2 a_0, compared to the smaller PAW projector radius of for Mn in VASP, which is 2.8 a_0. We defer a comparative discussion of average time per SCF iteration to Appendix C.

The benefit of this particular study is to show that SIRIUS can be used in "gold-standard" mode in studies of large molecular complexes, hence, to confirm, in particular, that our previous VASP calculations on the [Mn(taa)] complex were sufficiently accurate for the purpose.

IV. SIRIUS: Mn_3 DIMER MOLECULE

One highly desirable property to demonstrate for potential application of SMMs would be quantum mechanical coupling of two or more SMMs either to one other or to a surface or other device component, all the while retaining their isolated-molecule magnetic properties to a useful degree. For this, an SMM–SMM coupled structure was identified for hydrogen-bonded supramolecular pairs of $S = 9/2$ SMMs $[Mn_4O_3Cl_4(O_2CEt)_3(py)_3]$.[71–73] Since the hydrogen-bonded inter-SMM interactions do not provide easy control of oligomerization nor guarantee retention of the oligomeric structure in solution, covalently organic linked SMM–SMM structures were developed.

The first along that line was the $[Mn_3]_4$ SMM tetramer,[74] which is covalently linked with dioximate linker groups. A recent further development is the $[Mn_3]_2$ dimer molecule,[75] comprised of two Mn_3 units covalently joined via dpd2-dioximate linkers, as shown schematically in Fig. 3. The two triangular Mn_3 units are parallel and the inter-Mn_3 interaction has been determined to be ferromagnetic. There is no experimental evidence for noticeable interactions between the two Mn_3 units. That is consistent with the absence

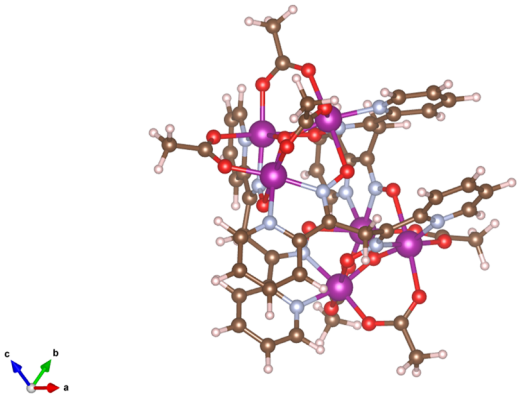

FIG. 3. Mn_3 dimer molecule.

of significant inter-Mn_3 contacts in the structure and the relatively large distance between Mn ions. The interaction quantum mechanically couples the two Mn_3 units. The structure is robust and resists any significant deformation or distortion that might affect the weak inter-Mn_3 coupling.

With the same consideration as for Mn[(taa)], we studied the isolated $[Mn_3]_2$ SMM dimer in a large periodically bounded box to be consistent with condensed phase calculations and to be assured of isolation. Note that $[Mn_3]_2$ has 137 atoms and 748 electrons, which is a much larger system then Mn[(taa)].

There is an important distinction. Both the $[Mn_3]_2$ SMM dimer and [Mn(taa)] calculations are done with a single *k*-point. Both relied upon the band parallelization in SIRIUS. The next two (see below) rely on that band parallelization as well. Both of those are metal-organic framework structures that do not have irregular vacuum regions and can use moderate Brillouin zone scan meshes and, hence, *k*-point parallelization as well. As with the [Mn(taa)] example, this $[Mn_3]_2$ SMM dimer calculation also benefits from the distributed storage of the *G*-vector related arrays.

Specifically, the molecule also was placed in a 20 Å periodically bounded box with single *k*-point Brillouin Zone sampling. The $G_{\max}$ cutoff and LO/*lo* configuration for the Mn atoms were the same as for [Mn(taa)], as shown in Table III. We also used the experimental geometry[75] and the PBE XC functional[69] (again, no Hubbard U). We are able to converge the system to the anti-ferromagnetic ground state in which there are two spin-up Mn and one spin-down Mn in each $[Mn_3]$ unit, and the total moment is zero.

The SIRIUS calculation yields similar values to those from VASP in the HOMO–LUMO gaps, which are almost identical. For the magnetization, the VASP value for the Mn ion is larger than what SIRIUS gives. Apparently, this is traceable to the muffin-tin radius (SIRIUS) being smaller than the projector cutoff radius (VASP). The average time consumed per SIRIUS SCF iteration is about 2.5 times larger than that for [Mn(taa)], but this is based on the same 16 MPI tasks for band parallelization. Increasing the number of tasks or number of cores per task would definitely make the job run faster. Comparison with VASP timings is in Appendix C. As with the previous study, this one shows that the SIRIUS APW+*lo* calculation can be used as a "gold-standard" to test and check VASP results.

TABLE III. Input parameters and outputs of the Mn_3 dimer.

Structure	Mn_3 dimer
Unit cell	$20 \times 20 \times 20$ Å^3 cubic
Number of atoms in unit cell	137
R_{mt} (a_0)	Mn: 2.2; O/N: 1.4; C: 1.2; H: 1.0;
$R_{\min}^{MT} \cdot \lvert \boldsymbol{G}^k \rvert_{\max}$	5
$\lvert \boldsymbol{G}_{\max} \rvert$ (a_0^{-1}) for ρ and V_{eff}	30
$l_{\max}$ for APW	8
$l_{\max}$ for ρ and V_{eff}	8
Size of basis set	≈165 300
k-point grid	$1 \times 1 \times 1$
(L)APW configuration	$\varepsilon_l = -0.15$ eV; $\partial_E = 0$;
lo configuration ⋆	Mn: s, p, d; O/C/N: s, p; H: s
Core state	Mn: 1s, 2s, 2p, 3s; O/C/N: 1s
Total energy tolerance	10^{-6} hartree
Potential tolerance	10^{-7} hartree
Run job setup:	16 MPI tasks
	16 OMP threads per task
Number of SCF iterations	125 (VASP: 86)
Average time per SCF iteration	≈250 s
HOMO-LUMO gap (eV)	0.26 (VASP: 0.27)
μ_{tot} (μ_B)	Each Mn atom (Sirius): ±1.92
	Each Mn atom (VASP): ±1.95

V. SIRIUS: DTN MOLECULE

The insulating organic compound XCl_2–$[SC(NH_2)_2]_4$ with X = Ni or Co (DTN or DTC molecule, respectively) is a molecule-based framework structure in which magnetic and electric order can couple. It has been studied experimentally for its quantum magnetism.[76–79] ($NiCl_2$–$[SC(NH_2)_2]_4$) has a tetragonal molecular crystal structure with two Ni atoms as magnetic centers in one unit cell. Each Ni has four S atoms and two Cl atoms as nearest neighbors, as shown in Fig. 4. They form an octahedral structure similar to the BO_6 octahedra in ABO_3 perovskites. The base octahedral structures pack in a body-centered tetragonal lattice, with Ni–Cl–Cl–Ni bonding along the c-axis (Fig. 4) and hydrogen bonding in the a–b-plane. The four thiourea $[SC(NH_2)_2]$ groups around each Ni ion are electrically polar. The a–b-plane components of their electric polarization cancel, while the c-axis components are in the same direction, thereby creating a net c-axis electric polarization that could be responsible for magnetic field-modified ferroelectricity.

At temperatures below 1.2 K and below a critical magnetic field, DTN is a quantum paramagnet.[80] As the magnetic field along the c-axis reaches the first critical value, DTN undergoes a quantum phase transition into an XY-antiferromagnetic state in which all Ni spins lie within the a–b plane. Upon further increase of the field, the spins begin to be more aligned with a corresponding increase in magnetization. When a second critical field is reached, the magnetization saturates and the material enters a spin-polarized state with all spins aligned parallel to the applied magnetic field.

There are three non-equivalent Ni–Ni spin couplings in the DTN bulk that are of interest: J_c along the c-axis (along the Ni–Cl–Cl–Ni bonding) between two Ni ions in adjacent unit cells, J_{ab} in the a–b- plane between two Ni ions in adjacent unit cells, and

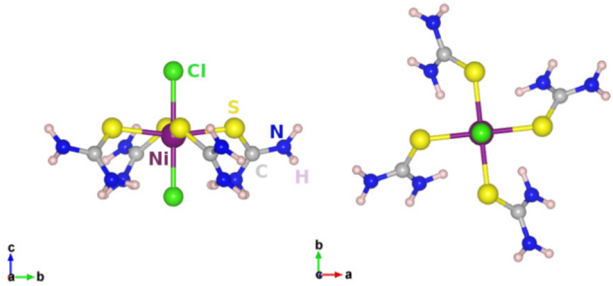

FIG. 4. The base octahedral unit of the DTN molecule.[80]

J_{diag} between the two Ni ions within one unit cell. Experiments suggest that the exchange coupling along the c-axis via the Ni–Cl–Cl–Ni chain is strong,[81] and the system behaves as a quasi-one-dimensional antiferromagnetic (AFM) chain of Ni^{2+} ions such that each ion has $S = 1$. DFT calculation can capture the main differences in values between the exchange coupling constants. A recent DFT+U study[80] showed that rather large Hubbard U correction (about 5–6 eV) is needed to match experimentally fit values of the coupling constants. However, the main feature, namely, that J_c is about an order of magnitude larger than J_{ab}, is already captured by ordinary KS-DFT calculations without the Hubbard U correction.

Thus, we calculated J_{ab} and J_c using SIRIUS without U. To estimate the J values, we first calculate the total energy of the ferromagnetic (FM) ordered and the AFM ordered states, E_{FM} and E_{AFM}, respectively. Then, assuming a Heisenberg Hamiltonian of the form $H = J[S_1 \cdot S_2]$, one can determine J from E_{FM}–E_{AFM}.[82] The calculation is done using supercells, $1 \times 1 \times 2$ for J_c and $2 \times 1 \times 1$ for J_{ab}. J_{diag} is obtained with the primitive unit cell. The supercells contain a number of atoms similar to that for the Mn_3-dimer molecule in the preceding example, namely, 140 atoms and 888 electrons. The size of the supercell is ~$10 \times 10 \times 20$ Å^3, about half of the cell used for both [Mn(taa)] and the Mn_3 dimer. Although the unit cell is smaller, we found that proper convergence in total energy still requires a high plane-wave cutoff, $|G_{\max}| = 25$–30 (a_0^{-1}), for the density and potential. The input parameters are listed in Table IV.

Using the APW+lo basis and with quality parameter $R_{\min}^{MT} \cdot |\boldsymbol{G}^k|_{\max} = 6$, we can get the converged paramagnetic (PM) ground state using the primitive unit cell and the AFM and FM ground states using $1 \times 1 \times 2$ and $2 \times 1 \times 1$ supercells. In the AFM and FM configurations, the calculated magnetic moment of Ni is slightly smaller than the VASP value. The J_{ab} and J_c determined from the differences in total energies, Table V, confirmed the observation obtained from using VASP. The ratio $J_{ab}/J_c \approx 8$ is actually slightly more significant than that determined by VASP, and both are in reasonable agreement with experiments. When using the primitive unit cell to determine J_{diag}, we found little differences in total energies of the FM and AFM ground state. This does not really conflict with the VASP observed 0.03 meV because the limit of the FLAPW accuracy (excluding approximations brought by XC functionals) is at 1 μhartree, which is exactly 0.027 meV. The VASP-observed very small J_{diag} could be within the PAW pseudo-potential approximation error bar.

TABLE IV. Input parameters and outputs of DTN.

Structure	DTN 1 × 1 × 2 supercell
Unit cell	≈ 10 × 10 × 20 Å^3 box
Number of atoms in unit cell	140
R_{mt} (a_0)	Na: 2.2; Cl/S/N: 1.4; C/H: 1.2;
$R_{\min}^{MT} \cdot \lvert \boldsymbol{G}^k \rvert_{\max}$	6
$\lvert \boldsymbol{G}_{\max} \rvert$ (a_0^{-1}) for ρ and V_{eff}	30
$l_{\max}$ for APW	8
$l_{\max}$ for ρ and V_{eff}	8
Size of basis set	≈189 500
k-point grid	2 × 2 × 2
(L)APW configuration for $l \le l_{\max}^{\text{APW}}$	$\varepsilon_l = -0.15$ eV; $\partial_E = 0$;
lo configuration	Na/Co: s, p, d
	Cl/S/C/N: s, p; H: s
Treated as core state	Ni/Co: 1s, 2s, 2p, 3s
	Cl/S/C/N: 1s
Total energy tolerance	10^{-7} hartree
Potential tolerance	10^{-7} hartree
Run job setup:	64 MPI tasks
	16 OMP threads per task
Number of SCF iterations	90 (VASP:70)
Average time per SCF iteration	≈450 s
HOMO–LUMO gap (eV)	0.18 (VASP: 0.18)
Magnetic moment	Ni atom: ±0.89 (VASP: ±0.92)

TABLE V. Exchange coupling constants from Sirius calculation compared to VASP results.[80]

	J_c (meV)	J_{ab} (meV)	J_{diag} (meV)
SIRIUS (DTN)	−2.72	−0.34	0.00
VASP (DTN)[80]	−1.05	−0.15	0.03

VI. SIRIUS: [Fe(tBu_2qsal)$_2$] MOLECULE

The [Fe(tBu_2qsal)$_2$] molecule is a recently created spin crossover metal–organic framework (MOF) structure,[83] as schematically shown in Fig. 5, where (tBu_2qsal) stands for 2,4-diterbutyl-6-((quinoline-8-ylimino)methyl)phenolate.

The crystallized structure was determined by x-ray diffraction to be monoclinic in space group $P2_1/c$. It is potentially a functional molecular magnetic material because [Fe(tBu_2qsal)$_2$] can be sublimed at 473–573 K and 10^{-3} to 10^{-4} mbar; hence, its thin-film deposition on a substrate is possible. The system undergoes a hysteretic spin transition. The average Fe–N and Fe–O bond lengths elongate from 1.949(2) Å at 100 K to 2.167(2) Å at 230 K and from 1.945(1) at 100 K to 1.997(1) Å at 230 K, respectively. These changes indicate that conversion from the LS ($S = 0$) to HS ($S = 2$) structure takes place as the temperature is increased. In addition, PW-PP-based DFT calculations[84] found that the electron transfer is minimal for the molecule on a monolayer of Au(111). It suggests very small changes in the electronic structure and magnetic properties when the molecule is placed on the surface of Au.

The unit cell of [Fe(tBu_2qsal)$_2$] contains 436 atoms and 2435 electrons. For a system of this size, we used $R_{\min}^{MT} \cdot G_{\max} = 4$. The

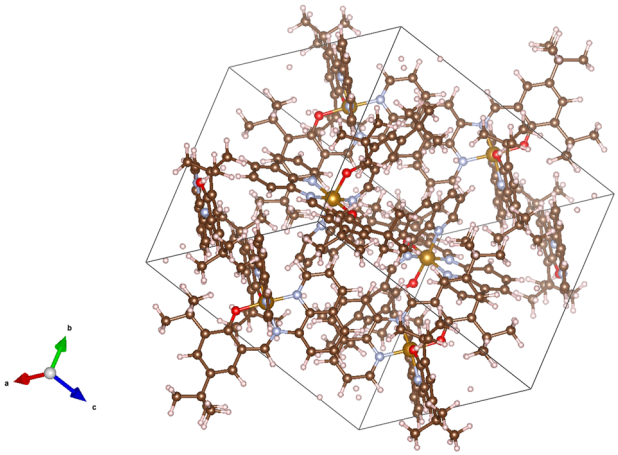

FIG. 5. The [Fe(tBu_2qsal)$_2$] MOF structure.

other cutoffs are basically same as the previous cases, as shown in Table VI.

The large number of atoms does not make the Hamiltonian matrix dimension significantly larger than in the preceding cases, but it makes the calculation much more time consuming. This is because the total number of radial functions of the APW functions linearly increases with the number of atoms. For each muffin-tin, the radial functions are normally expanded up to $l = 8$ in comparison with the β projectors[85,86] of the pseudo-potential method, which

TABLE VI. Input parameters of the Fe_4 molecule, $S = 0$.

Structure	Fe_4 MOF
Unit cell	15 × 16 × 17.5 Å^3
Number of atoms in unit cell	436
R_{mt} (a_0)	Fe: 2.2; O: 1.4; C: 1.2; H: 1.0;
$R_{\min}^{MT} \cdot \lvert \boldsymbol{G}^k \rvert_{\max}$	4
$\lvert \boldsymbol{G}_{\max} \rvert$ (a_0^{-1}) for ρ and V_{eff}	30
$l_{\max}$ for APW	8
$l_{\max}$ for ρ and V_{eff}	8
Size of basis set	≈160 500
k-point grid	1 × 1 × 1
(L)APW configuration	$\varepsilon_l = -0.15$ eV; $\partial_E = 0$;
lo configuration ⋆	Fe: s, p, d
	Cl/S/C/N: s, p; H: s
Treated as core state	Ni/Co: 1s, 2s, 2p, 3s
	Cl/S/C/N: 1s
Total energy tolerance	10^{-6} hartree
Potential tolerance	10^{-7} hartree
Run job setup:	64 MPI tasks
	16 cores per task
	16 OMP threads per task
Number of SCF iterations	135
Average time per SCF iteration	≈2150 s

typically are defined for *s*, *p*, and *d* states only. In each SCF iteration, diagonalization of the Hamiltonian involves repeated application of the Hamiltonian to a set of wave functions. That requires summation over the APW radial functions, a task that becomes a major time consuming operation when treating large systems using APW+*lo*. For this MOF structure, we used the experimental structure and single *k*-point Brillouin zone sampling. $R_{\text{min}}^{MT} \cdot |\boldsymbol{G}^{k}|_{max}$ was set to 4. The plane wave cutoffs for density and potential were set to 30, as before, and the angular momentum cutoff was set to the normal value, 8. Maximum benefit of band parallelization on the NERSC CORI machine (which has two 16-core CPUs and total 128 GB memory per node) is reached at 8 × 8 MPI tasks. Each task is assigned with the resources of 16 cores; thus, two tasks occupy one node, which is tested to be optimal. Further increasing the number of tasks, or assigning more resources to each task, does not seem to accelerate the calculation. With the setup described, we managed to converge the system to non-magnetic ground state in about 80 h. The total time needed to converge to the ground state also depends on the number of SCF iterations, which depends on the mixing algorithm for the charge density. The mixing algorithm used in the present work is the Broyden scheme[87] in which the Jacobian matrix is approximated from the previous step and improved iteratively. Other mixing schemes that implicitly approximate the inverse Jacobian from multiple previous steps, e.g., the Anderson mixing scheme,[88] are being tested. However, adjusting and testing the mixing parameter or any other input parameter using a system of this size is not really practical, simply as a matter of resource availability. Thus, the calculation of this MOF structure is a feasibility test only. We have shown that meaningful KS-DFT calculations *can be done* on a system of this size using APW+*lo* and have confirmed the computational cost advantage of efficient job distribution.

VII. SUMMARY AND CONCLUSION

The main purpose of this work is to demonstrate, by several concrete examples, the value of the SIRIUS architecture and implementation for all-electron KS-DFT calculations on fairly large molecules with complicated spin manifolds. By inference, this capacity extends to aggregates of such systems. SIRIUS as a stand-alone package provides performance gains through refined diagonalization methods and task and data parallelization improvements. The result is an advance in capability of the APW+*lo* DFT treatment of complex molecular aggregates.

To recapitulate, the eigenvalue solver and the distribution of *G*-vector arrays in community FLAPW codes, for example, ELK, *exciting*, and Exciting-Plus, are major bottleneck in calculations of large systems. The LAPACK/ScaLAPACK full diagonalization algorithm cannot handle Hamiltonian matrices larger than $\approx 10^6$, and the *G*-vector arrays cannot be handled efficiently without distributed storage. The SIRIUS package provides better data distribution and options to the use of the various (LAPACK, ScaLAPACK, and Davidson) diagonalization algorithms. One can perform Davidson-type diagonalization of the Hamiltonian easily in the self-consistent loop and benefit from multiple MPI and thread-level parallelization within *k*-points and within bands. Together with the proper distribution of *G*-vector related arrays, the SIRIUS package can do plane wave based LAPW and APW+*lo* calculation of systems larger than many community LAPW/APW+*lo* codes.

We showed results from molecules using the APW+*lo* basis. The resulting total energy and magnetization are in agreement with experimental measurements and confirm corresponding VASP calculations done with PAWs. In these test calculations, good scaling in band parallelization is observed, which is particularly crucial for a single *k*-point calculations ([Mn(taa)], Mn_3 dimer). The results also indicate that SIRIUS parallelization works well on contemporary high performance systems, and the computational time is drastically reduced compared to ELK and Exciting-Plus, for example. For a system of the size of the DTN supercell studied in this work, the main physical feature is captured by extraction of exchange constants *J* from the total energies. The results are qualitatively in agreement with experiment and VASP calculations.

Looking ahead, all-electron FLAPW and APW+*lo* calculations of medium to large molecule and MOF systems is a relatively little-explored area. It is plausible that important core effects from, for example, spin–orbit coupling will be uncovered by such all-electron investigations. At the least, the use of plane-wave-PAW codes to drive *ab initio* BOMD will be validated at sample configurations by such all-electron calculations. We have shown that the SIRIUS package can handle systems as large as 200 non-H atoms routinely without losing the accuracy needed for magnetic systems. With suitable high-performance systems, SIRIUS demonstrably can be used for systems up to 430 atoms and, we surmise, larger.

ACKNOWLEDGMENTS

This work was supported as part of the Center for Molecular Magnetic Quantum Materials, an Energy Frontier Research Center funded by the U.S. Department of Energy, Office of Science, Basic Energy Sciences under Award No. DE-SC0019330. Computations were performed at the NERSC and the University of Florida Research Computer Center.

AUTHOR DECLARATIONS

Conflict of Interest

The authors have no conflicts to disclose.

Author Contributions

Long Zhang: Conceptualization (equal); Data curation (lead); Formal analysis (lead); Methodology (lead); Writing – original draft (lead); Writing – review & editing (equal). **Anton Kozhevnikov**: Conceptualization (equal); Methodology (equal); Software (lead). **Thomas Schulthess**: Conceptualization (equal); Methodology (equal); Software (lead). **S. B. Trickey**: Conceptualization (equal); Formal analysis (equal); Funding acquisition (equal); Project administration (equal); Supervision (equal); Writing – original draft (equal); Writing – review & editing (equal). **Hai-Ping Cheng**: Conceptualization (equal); Formal analysis (equal); Funding acquisition (lead); Project administration (equal); Resources (lead); Supervision (lead); Writing – original draft (equal); Writing – review & editing (equal).

DATA AVAILABILITY

The source code and data that support the findings of this study are openly available in GitHub repository https://github.com/electronic-structure/SIRIUS.

APPENDIX A: SOME IMPLEMENTATION DETAILS OF SIRIUS

The development of SIRIUS library aimed originally to find and isolate major performance bottlenecks in the ground state calculations of the Exciting and ELK codes. Later, the functionality of the library was extended to support the pseudopotential method, and the API for Fortran code was proposed. The SIRIUS library is essentially a collection of C++14 classes that abstract away the different building blocks of PP-PW and FP-LAPW codes.

It comes with the CUDA[89] backend to provide several features: (1) low-level support, such as pointer arithmetic and type casting, and high-level abstractions, such as classes and template metaprogramming; (2) easy interoperability between C++ and widely used Fortran90; (3) full support from the standard template library (STL);[90] and (4) easy integration with the CUDA nvcc compiler.[91] Although not relevant here, SIRIUS provides dedicated Fortran API functions for interfacing to the QuantumEspresso and *exciting* codes.

The class composition hierarchy starts from the most primitive classes, such as `Communicator`, `Eigen_Solver`, `Basis_Descriptor`, and `Spline`, and high-level classes for DFT, such as `Band`, `Density`, `Potential`, and `DFT_ground_state`. The code is written in C++14 with MPI, OpenMP, and CUDA programming models. The Fortran90 API is provided through the standard `ISO_C_BINDING` mechanism. The SIRIUS library is available[92] open source and is distributed under BSD-2-Clause license. Below, we give a short description of the most important SIRIUS classes.

1. `Simulation_context` *class*:

This class is used to store the parameters of a single calculation. It contains the information about the unit cell, reciprocal lattice, G-vectors, FFTs, MPI communicators, and various run-time options that control the simulation. The initialized instance of this class is passed to the high level classes, such as `Band`, `Density`, and `Potential`.

2. `Wave_function` *class*:

This class is used for handling the scalar or spinor wave functions, which are described by a set of plane wave and radial function expansion coefficients. Since the MT part of the LAPW functions and the LO or *lo* functions are all constructed from linear combination of radial functions and its energy derivatives multiplied with spherical harmonics, we use one object $f^{\alpha}_{lv}(r)$ to represent them. The wave function expansion can be written as the plane wave part plus the MT part,

$$\psi^{\sigma}_{i\boldsymbol{k}}(\boldsymbol{r}) = (1/\sqrt{\Omega})\sum_{G}^{\boldsymbol{r}\notin\alpha} C^{\sigma}_{i\boldsymbol{k}}(\boldsymbol{G})e^{i(\boldsymbol{G}+\boldsymbol{k})\cdot\boldsymbol{r}} + \sum_{\alpha}^{\boldsymbol{r}\in\alpha}\sum_{\{lvm\}} C^{\sigma}_{i\boldsymbol{k}}(\alpha,\{lvm\})f^{\alpha}_{lv}(r)Y_{lm}(\hat{\boldsymbol{r}}), \tag{A1}$$

where α is the MT indices, l and m are the angular momentum quantum number and the azimuthal quantum number, and v is the order index of a LO/*lo* or MT part of LAPW function for a given l.

The expansion coefficients are stored as a matrix for each of the spinor components. The leading dimension is the row index, which represents the basis functions. The column index represents the Kohn–Sham orbitals (bands). The wave function is stored between MPI ranks in the distributed way where the column (band) index remains whole and the row (basis) index is divided between the ranks.

The SIRIUS implements three basic functions to perform linear algebra operations on the distributed wave functions. (1) `inner()`: it computes the inner product between two wave functions $O_{ij} = \langle\Psi_i|\Psi_j\rangle$. The resulting overlap matrix can be global or distributed in ScaLAPACK 2D block-cyclic fashion. (2) `transform()`: it computes a general linear transformation of the wave function $|\Psi_i\rangle = \sum_{ij} M_{ij}|\phi_j\rangle$. Similarly, the transformed matrix can be global or distributed in 2D block-cyclic distribution. (3) `orthogonalize()`: it orthonormalizes the wave functions with the fast block Gram–Schmidt procedure.

On a regular grid, wave functions are Fourier-transformed to a real-space domain, and their contribution is added to the density and magnetization in a straightforward manner.

3. `Density` *class*:

This class is used to generate charge density $\rho(\boldsymbol{r})$ and magnetization $\boldsymbol{m}(\boldsymbol{r})$ on the regular grid and inside the MT spheres,

$$\rho_{\sigma\sigma'}(\boldsymbol{r}) = \sum_{i\boldsymbol{k}}^{occ.} n_{i\boldsymbol{k}}\psi^{\sigma *}_{i\boldsymbol{k}}(\boldsymbol{r})\psi^{\sigma'}_{i\boldsymbol{k}}(\boldsymbol{r}) = \frac{1}{2}\begin{bmatrix} \rho(\boldsymbol{r}) + m_z(\boldsymbol{r}) & m_x(\boldsymbol{r}) - im_y(\boldsymbol{r}) \\ m_x(\boldsymbol{r}) + im_y(\boldsymbol{r}) & \rho(\boldsymbol{r}) - m_z(\boldsymbol{r}) \end{bmatrix}. \tag{A2}$$

For FP-LAPW calculation, one needs to find the spherical expansion of the charge density inside the MT spheres. It is obtained by first calculating the occupancy matrix for each MT from the MT part of the wave function expansion coefficients, then reducing over the angular momentum quantum numbers with the Gaunt coefficients and then using the radial functions and the occupancy matrix to get the spherical expansion of the MT charge density.

4. `Band` *class*:

This class is used to solve the Kohn–Sham equations,

$$-\frac{1}{2}\nabla^2\psi^{\sigma}_{i\boldsymbol{k}} + \sum_{\sigma'}\hat{V}_{\sigma\sigma'}\psi^{\sigma'}_{i\boldsymbol{k}} = \varepsilon_{i\boldsymbol{k}}\psi^{\sigma}_{i\boldsymbol{k}}. \tag{A3}$$

For spin-polarized DFT, the total effective potential is a two-by-two matrix acting on spinor wave functions. The potential contains the scalar effective potential $v_{eff}(\boldsymbol{r})$, the effective magnetic field potential $B(\boldsymbol{r})$, and the non-local part of the pseudo-potential for pseudo potential calculations,

$$\hat{V}_{\sigma\sigma'} = \begin{bmatrix} v_{eff}(\boldsymbol{r}) + B_z(\boldsymbol{r}) & B_x(\boldsymbol{r}) - iB_y(\boldsymbol{r}) \\ B_x(\boldsymbol{r}) + iB_y(\boldsymbol{r}) & v_{eff}(\boldsymbol{r}) - B_z(\boldsymbol{r}) \end{bmatrix} + \sum_{\alpha} \sum_{nn'} |\beta_n^{\alpha}\rangle D^{\alpha}_{n\sigma,n'\sigma'} \langle \beta_{n'}^{\alpha}|. \quad \text{(A4)}$$

Here, $|\beta_n^{\alpha}\rangle$ is the so-called "beta-projectors" of the pseudopotential method defined for each atom α. The eigen value problem is then solved using full diagonalization of LAPACK/ScaLAPACK or the Davidson type iterative diagonalization.

5. `Potential` ***class***:

This class is used to generate the scalar effective potential and the exchange–correlation magnetic field from the charge density and magnetization on the regular FFT grid and inside the muffin-tin spheres,

$$\begin{aligned} v(\boldsymbol{r}) &= v_{ext}(\boldsymbol{r}) + v_H(\boldsymbol{r}) + v_{XC}(\boldsymbol{r}), \\ v_H(\boldsymbol{r}) &= \frac{1}{2} \int \frac{\rho(\boldsymbol{r}')}{|\boldsymbol{r} - \boldsymbol{r}'|} d\boldsymbol{r}', \\ v_{XC}(\boldsymbol{r}) &= \frac{\delta E_{XC}[\rho(\boldsymbol{r}), m(\boldsymbol{r})]}{\delta \rho(\boldsymbol{r})}, \end{aligned} \quad \text{(A5)}$$

where $m(\boldsymbol{r})$ is the absolute value of the magnetization.

The current version of SIRIUS only has native implementation of L(S)DA and GGA building, which relies on interfacing to the LibXC. It follows the standard procedure to interact with LibXC: First, the gradient and the Laplacian of the real space charge density $n(\boldsymbol{r})$ are obtained in spectral representation ($\boldsymbol{G}$ space); then, they are Fourier transformed back to the real space grid. Second, the contracted gradient $\sigma \equiv |\nabla n(\boldsymbol{r})|^2$ is prepared, and both $n(\boldsymbol{r})$ and σ are supplied to LibXC to get $\partial\varepsilon_{xc}/\partial\sigma$ and $\partial\varepsilon_{xc}/\partial n$ in return. Finally, the quantity $\partial\varepsilon_{xc}/\partial\sigma$ needs to be transformed to spectral representation to get its gradient and the gradient be transformed back to the real space grid.

The standalone SIRIUS calculation, either FP-LAPW or PP-PW, currently does not support hybrid functionals.

APPENDIX B: MAGNETISM AND SPIN–ORBIT COUPLING IN SIRIUS FULL POTENTIAL CALCULATION

The FP-LAPW calculation in SIRIUS is implemented in the first-variation-then-second-variation way. The Kohn–Sham equations are first solved for a spin-independent Hamiltonian in the first-variation stage. In the second-variation stage, magnetic states are explored with adding a perturbing external magnetic field B_{ext} to the paramagnetic state. The perturbing B_{ext} is gradually turned off in the self-consistent cycle, allowing the system to converge to possible magnetic states. The calculations done in this work are within this vanishing B_{ext} approach. It has not been implemented but is planned for the alternative scheme where the external B_{ext} can be adjusted in such a way that a desirable constant magnetic moment can be maintained throughout the self-consistent cycle.

When the spin–orbit coupling (SOC) needs to be considered, it is commonly accepted in muffin-tin based DFT codes that the SOC is significant only near the nuclear centers contained inside the muffin-tins; thus, a spherical potential is sufficient for describing the interaction. SIRIUS adopts this approximation and treats SOC only inside the muffin-tins in the second-variation stage. The valence electrons in the muffin-tins are by default already treated in the scalar relativistic zero-order regular approximation (ZORA) to the Dirac equation. Thus, turning on SOC means adding a $\boldsymbol{\sigma} \cdot \boldsymbol{L}$ term to the second-variation Hamiltonian, and in such a way, it is also consistent with the spin densities of traditional XC functionals.

APPENDIX C: TIMING COMPARISON

Caution must be exercised in interpreting what follows. This is because comparison of computational costs between conceptually and structurally distinct codes is a task fraught with difficulties. Optimal resource assignments generally differ greatly not only between codes but among different machine configurations. Both the definitions and effects of precision tolerances differ between codes as well.

We compare SIRIUS only with VASP because of its very wide use and because of the cost of running the large systems studied here with other PW-PP codes. Even this restriction to one comparison involves some critical choices. Begining with MPI parallelization, we can force the two codes to run with the same number of MPI tasks, but the situations for each task are very different. The discussion that follows is specific to the NERSC Cori machine.

By experiment, we have found that the optimum number of OpenMP threads per task for SIRIUS is 16. To obtain adequate memory per task, it is also necessary to assign no more than two tasks on a node. Putting more than two on a single node degrades performance noticeably.

In contrast, for VASP, the recommended practice does not require the use of OpenMP. If, however, we use openMP for the sake of even-handed comparison, experiment showed that ordinarily four openMP threads per task generally is optimum (with eight at most). Thus, we can put four or more tasks per node.

Our testing was for the two systems reported above, [Mn(taa)] and Mn_3 dimer. For both, we did single k-point calculations at fixed geometries with 16 MPI tasks and optimal OpenMP threads per task for each code. The choice of diagonalizer is unique in SIRIUS but not in VASP. In it, the better choice appears to be the tag "ALGO = Fast," which invokes a mixture of the Davidson and RMM-DIIS algorithms.

With these choices, the results are that the ratio of average time per SCF iteration for VASP vs SIRIUS is about 50% for [Mn(taa)] and about 25% for the Mn_3 dimer. For [Mn(taa)], the iteration count is 75 for SIRIUS and 55 for VASP, so the rough computational cost of SIRIUS vs VASP is about a factor of 2.7. For the Mn_3 dimer, the iteration counts are 125 (SIRIUS) and 90 (VASP), so the computational cost ratio is about 5.6.

The use of the VASP "ALGO = normal" option, which invokes a blocked Davidson diagonalization algorithm, increases the VASP iteration count by about 10%, so the ratios become roughly 2.4 and 5.1, respectively.

Of course, these cost ratios refer to different numbers of electrons, since SIRIUS is all-electron, while VASP uses PAWs. For [Mn(taa)], the electron count is 224 vs 156 (SIRIUS and VASP, respectively), while for the Mn_3 dimer, the counts are 748 and 510, respectively. If cubic scaling with electron number (which is the most

elementary expectation with Kohn–Sham calculations) is followed, the [Mn(taa)] ratio would be 2.96, not far from the observed 2.7. For Mn_3, however, cubic scaling would give 3.16. Apparently, the actual 5.6 is a consequence of parallelization, but we have not investigated the matter.

The larger point is that the cost-scaling, though significant, is not prohibitive even for quite large molecular systems. With that established, Secs. V and VI had given two more illustrative examples of the use of SIRUS in the context of molecular magnetic quantum materials.

REFERENCES

[1] M. R. Wasielewski, M. D. E. Forbes, N. L. Frank, K. Kowalski, G. D. Scholes, J. Yuen-Zhou, M. A. Baldo, D. E. Freedman, R. H. Goldsmith, T. Goodson III, M. L. Kirk, J. K. McCusker, J. P. Ogilvie, D. A. Shultz, S. Stoll, and K. B. Whaley, "Exploiting chemistry and molecular systems for quantum information science," Nat. Rev. Chem. **4**, 490–504 (2020).

[2] A. Gaita-Ariño, F. Luis, S. Hill, and E. Coronado, "Molecular spins for quantum computation," Nat. Chem. **11**, 301–309 (2019).

[3] S. L. Castro, Z. Sun, C. M. Grant, J. C. Bollinger, D. N. Hendrickson, and G. Christou, "Single-molecule magnets: Tetranuclear vanadium(III) complexes with a butterfly structure and an $S = 3$ ground state," J. Am. Chem. Soc. **120**, 2365–2375 (1998).

[4] R. Bagai and G. Christou, "The *Drosophila* of single-molecule magnetism: $[Mn_{12}O_{12}(O_2CR)_{16}(H_2O)_4]$," Chem. Soc. Rev. **38**, 1011–1026 (2009).

[5] K. P. Kepp, "Consistent descriptions of metal–ligand bonds and spin-crossover in inorganic chemistry," Coord. Chem. Rev. **257**, 196–209 (2013).

[6] J. Cirera, M. Via-Nadal, and E. Ruiz, "Benchmarking density functional methods for calculation of state energies of first row spin-crossover molecules," Inorg. Chem. **57**, 14097–14105 (2018).

[7] K. P. Kepp, "The electronic determinants in spin crossover described by density functional theory," in *Transition Metals in Coordination Environments*, Challenges and Advances in Computational Chemistry and Physics Vol. 29, edited by E. Broclawik, T. Borowski, and M. Radoń (Springer, 2019), pp. 1–33.

[8] D. Mejía-Rodríguez, A. Albavera-Mata, E. Fonseca, D.-T. Chen, H.-P. Cheng, R. G. Hennig, and S. B. Trickey, "Barriers to predictive high-throughput screening for spin-crossover," Comput. Mater. Phys. **206**, 111161 (2022).

[9] C. H. Marrows, L. C. Chapon, and S. Langridge, "Spintronics and functional materials," Mater. Today **12**, 70–77 (2009).

[10] J. R. Friedman and M. P. Sarachik, "Single molecule nanomagnets," Annu. Rev. Condens. Matter Phys. **1**, 109–128 (2010).

[11] P. L. Feng and D. N. Hendrickson, "Isostructural single-chain and single-molecule magnets," Inorg. Chem. **49**, 6393–6395 (2010).

[12] J. L. Rong-Min Wei and F. Cao, "Single-chain magnets based on octacyanotungstate with the highest energy barriers for cyanide compounds," Sci. Rep. **6**, 24372 (2016).

[13] L.-M. Zheng, J. Tang, H.-L. Sun, and M. Ren, "Low dimensional molecular magnets and spintronics," in *Handbook of Spintronics*, edited by Y. Xu, D. D. Awschalom, and J. Nitta (Springer Netherlands, Dordrecht, 2016), pp. 617–680.

[14] A. E. Thorarinsdottir and T. D. Harris, "Metal–organic framework magnets," Chem. Rev. **120**, 8716–8789 (2020).

[15] M. Kurmoo, "Magnetic metal–organic frameworks," Chem. Soc. Rev. **38**, 1353–1379 (2009).

[16] L. Bogani and W. Wernsdorfer, "Molecular spintronics using single-molecule magnets," Nat. Mater. **7**, 179–186 (2008).

[17] J. Gómez-Segura, J. Veciana, and D. Ruiz-Molina, "Advances on the nanostructuration of magnetic molecules on surfaces: The case of single-molecule magnets (SMM)," Chem. Commun. **2007**, 3699–3707.

[18] G. Mínguez Espallargas and E. Coronado, "Magnetic functionalities in MOFs: From the framework to the pore," Chem. Soc. Rev. **47**, 533–557 (2018).

[19] J. M. Frost, K. L. M. Harriman, and M. Murugesu, "The rise of 3-d single-ion magnets in molecular magnetism: Towards materials from molecules?," Chem. Sci. **7**, 2470–2491 (2016).

[20] K. Ziemelis, "The difficult middle ground," Nat. Phys. **4**, S19 (2008).

[21] R. F. Weinland and G. Fischer, "Über manganiacetate und -benzoate," Z. Anorg. Allg. Chem. **120**, 161–180 (1921).

[22] T. Lis, "Preparation, structure, and magnetic properties of a dodecanuclear mixed-valence manganese carboxylate," Acta Crystallogr., Sect. B: Struct. Crystallogr. Cryst. Chem. **36**, 2042–2046 (1980).

[23] P. D. W. Boyd, Q. Li, J. B. Vincent, K. Folting, H. R. Chang, W. E. Streib, J. C. Huffman, G. Christou, and D. N. Hendrickson, "Potential building blocks for molecular ferromagnets: $[Mn_{12}O_{12}(O_2CPh)_{16}(H_2O)_4]$ with a $S = 14$ ground state," J. Am. Chem. Soc. **110**, 8537–8539 (1988).

[24] A. Caneschi, D. Gatteschi, R. Sessoli, A. L. Barra, L. C. Brunel, and M. Guillot, "Alternating current susceptibility, high field magnetization, and millimeter band EPR evidence for a ground $S = 10$ state in $[Mn_{12}O_{12}(CH_3COO)_{16}(H_2O)_4]\cdot 2CH_3COOH\cdot 4H_2O$," J. Am. Chem. Soc. **113**, 5873–5874 (1991).

[25] R. Sessoli, H. L. Tsai, A. R. Schake, S. Wang, J. B. Vincent, K. Folting, D. Gatteschi, G. Christou, and D. N. Hendrickson, "High-spin molecules: $[Mn_{12}O_{12}(O_2CR)_{16}(H_2O)_4]$," J. Am. Chem. Soc. **115**, 1804–1816 (1993).

[26] E. Cremades, J. Cano, E. Ruiz, G. Rajaraman, C. J. Milios, and E. K. Brechin, "Theoretical methods enlighten magnetic properties of a family of Mn_6 single-molecule magnets," Inorg. Chem. **48**, 8012–8019 (2009).

[27] E. Ruiz, T. Cauchy, J. Cano, R. Costa, J. Tercero, and S. Alvarez, "Magnetic structure of the large-spin Mn_{10} and Mn_{19} complexes: A theoretical complement to an experimental milestone," J. Am. Chem. Soc. **130**, 7420–7426 (2008).

[28] O. Waldmann, A. M. Ako, H. U. Güdel, and A. K. Powell, "Assessment of the anisotropy in the molecule Mn_{19} with a high-spin ground state $S = 83/2$ by 35 GHz electron paramagnetic resonance," Inorg. Chem. **47**, 3486–3488 (2008).

[29] E. E. Moushi, T. C. Stamatatos, W. Wernsdorfer, V. Nastopoulos, G. Christou, and A. J. Tasiopoulos, "A family of 3D coordination polymers composed of Mn_{19} magnetic units," Angew. Chem., Int. Ed. **45**, 7722–7725 (2006).

[30] M. Murugesu, S. Takahashi, A. Wilson, K. A. Abboud, W. Wernsdorfer, S. Hill, and G. Christou, "Large Mn_{25} single-molecule magnet with spin $S = 51/2$: Magnetic and high-frequency electron paramagnetic resonance spectroscopic characterization of a giant spin state," Inorg. Chem. **47**, 9459–9470 (2008).

[31] M. Murugesu, M. Habrych, W. Wernsdorfer, K. A. Abboud, and G. Christou, "Single-molecule magnets: A Mn_{25} complex with a record $S = 51/2$ spin for a molecular species," J. Am. Chem. Soc. **126**, 4766–4767 (2004).

[32] P. Abbasi, K. Quinn, D. I. Alexandropoulos, M. Damjanović, W. Wernsdorfer, A. Escuer, J. Mayans, M. Pilkington, and T. C. Stamatatos, "Transition metal single-molecule magnets: A Mn_{31} nanosized cluster with a large energy barrier of 60 K and magnetic hysteresis at 5 K," J. Am. Chem. Soc. **139**, 15644–15647 (2017).

[33] A. J. Tasiopoulos, A. Vinslava, W. Wernsdorfer, K. A. Abboud, and G. Christou, "Giant single-molecule magnets: A Mn_{84} torus and its supramolecular nanotubes," Angew. Chem., Int. Ed. **43**, 2117–2121 (2004).

[34] R. Hernández Sánchez and T. A. Betley, "Meta-atom behavior in clusters revealing large spin ground states," J. Am. Chem. Soc. **137**, 13949–13956 (2015).

[35] C. Sangregorio, T. Ohm, C. Paulsen, R. Sessoli, and D. Gatteschi, "Quantum tunneling of the magnetization in an iron cluster nanomagnet," Phys. Rev. Lett. **78**, 4645–4648 (1997).

[36] A. K. Powell, S. L. Heath, D. Gatteschi, L. Pardi, R. Sessoli, G. Spina, F. Del Giallo, and F. Pieralli, "Synthesis, structures, and magnetic properties of Fe_2, Fe_{17}, and Fe_{19} oxo-bridged iron clusters: The stabilization of high ground state spins by cluster aggregates," J. Am. Chem. Soc. **117**, 2491–2502 (1995).

[37] C. Cadiou, M. Murrie, C. Paulsen, V. Villar, W. Wernsdorfer, and R. E. P. Winpenny, "Studies of a nickel-based single molecule magnet: Resonant quantum tunnelling in an $S = 12$ molecule," Chem. Commun. **2001**, 2666–2667.

[38] M. Murrie, S. J. Teat, H. Stœckli-Evans, and H. U. Güdel, "Synthesis and characterization of a cobalt(II) single-molecule magnet," Angew. Chem., Int. Ed. **42**, 4653–4656 (2003).

[39] Y.-Z. Zhang, W. Wernsdorfer, F. Pan, Z.-M. Wang, and S. Gao, "An azido-bridged disc-like heptanuclear cobalt(II) cluster: Towards a single-molecule magnet," Chem. Commun. **2006**, 3302–3304.

[40]A.-L. Barra, P. Debrunner, D. Gatteschi, C. E. Schulz, and R. Sessoli, "Superparamagnetic-like behavior in an octanuclear iron cluster," Europhys. Lett. **35**, 133–138 (1996).
[41]O. Waldmann, "A criterion for the anisotropy barrier in single-molecule magnets," Inorg. Chem. **46**, 10035–10037 (2007).
[42]F. Neese and D. A. Pantazis, "What is not required to make a single molecule magnet," Faraday Discuss. **148**, 229–238 (2011).
[43]H. Oshio and M. Nakano, "High-spin molecules with magnetic anisotropy toward single-molecule magnets," Chem. - Eur. J. **11**, 5178–5185 (2005).
[44]E. Ruiz, J. Cirera, J. Cano, S. Alvarez, C. Loose, and J. Kortus, "Can large magnetic anisotropy and high spin really coexist?," Chem. Commun. **2008**, 52–54.
[45]L. M. C. Beltran and J. R. Long, "Directed assembly of metal-cyanide cluster magnets," Acc. Chem. Res. **38**, 325–334 (2005).
[46]X.-Y. Wang, C. Avendaño, and K. R. Dunbar, "Molecular magnetic materials based on 4d and 5d transition metals," Chem. Soc. Rev. **40**, 3213–3238 (2011).
[47]K. S. Pedersen, J. Bendix, and R. Clérac, "Single-molecule magnet engineering: Building-block approaches," Chem. Commun. **50**, 4396–4415 (2014).
[48]D. N. Woodruff, R. E. P. Winpenny, and R. A. Layfield, "Lanthanide single-molecule magnets," Chem. Rev. **113**, 5110–5148 (2013).
[49]F.-S. Guo, A. K. Bar, and R. A. Layfield, "Main group chemistry at the interface with molecular magnetism," Chem. Rev. **119**, 8479–8505 (2019).
[50]R. Sessoli and A. K. Powell, "Strategies towards single molecule magnets based on lanthanide ions," Coord. Chem. Rev. **253**, 2328–2341 (2009), Deutsche Forschungsgemeinschaft Molecular Magnetism Research Report.
[51]S. G. McAdams, A.-M. Ariciu, A. K. Kostopoulos, J. P. S. Walsh, and F. Tuna, "Molecular single-ion magnets based on lanthanides and actinides: Design considerations and new advances in the context of quantum technologies," Coord. Chem. Rev. **346**, 216–239 (2017).
[52]Z. Zhu, M. Guo, X.-L. Li, and J. Tang, "Molecular magnetism of lanthanide: Advances and perspectives," Coord. Chem. Rev. **378**, 350–364 (2019), part of Special Issue: 8th Chinese Coordination Chemistry Conference.
[53]A. Dey, J. Acharya, and V. Chandrasekhar, "Heterometallic 3d–4f complexes as single-molecule magnets," Chem. - Asian J. **14**, 4433–4453 (2019).
[54]S. Demir, I.-R. Jeon, J. R. Long, and T. D. Harris, "Radical ligand-containing single-molecule magnets," Coord. Chem. Rev. **289-290**, 149–176 (2015).
[55]R. A. Layfield, "Organometallic single-molecule magnets," Organometallics **33**, 1084–1099 (2014).
[56]W. Kohn and L. J. Sham, "Self-consistent equations including exchange and correlation effects," Phys. Rev. **140**, A1133–A1138 (1965).
[57]E. Engel and R. M. Dreizler, *Density Functional Theory* (Springer, 2013).
[58]P. Hohenberg and W. Kohn, "Inhomogeneous electron gas," Phys. Rev. **136**, B864–B871 (1964).
[59]J. C. Slater, "Wave functions in a periodic potential," Phys. Rev. **51**, 846–851 (1937).
[60]J. C. Slater, *Energy Band Calculations by the Augmented Plane Wave Method* (Academic Press, 1964), pp. 35–58.
[61]O. K. Andersen, "Linear methods in band theory," Phys. Rev. B **12**, 3060–3083 (1975).
[62]D. D. Koelling and G. O. Arbman, "Use of energy derivative of the radial solution in an augmented plane wave method: Application to copper," J. Phys. F: Met. Phys. **5**, 2041–2054 (1975).
[63]L. Zhang, A. Kozhevnikov, T. Schulthess, H.-P. Cheng, and S. B. Trickey, "Performance enhancement of APW+*lo* calculations by simplest separation of concerns," Computation **10**, 43 (2022).
[64]E. Angerson, Z. Bai, J. Dongarra, A. Greenbaum, A. McKenney, J. Du Croz, S. Hammarling, J. Demmel, C. Bischof, and D. Sorensen, "LAPACK: A portable linear algebra library for high-performance computers," in *Supercomputing '90: Proceedings of the 1990 ACM/IEEE Conference on Supercomputing* (IEEE, 1990), pp. 2–11.
[65]A. Gulans *et al.*, "exciting: a full-potential all-electron package implementing density-functional theory and many-body perturbation theory," J. Phys.: Condens. Matter **26**, 363202 (2014).
[66]P. G. Sim and E. Sinn, "First manganese(III) spin crossover, first d4 crossover. Comment on cytochrome oxidase," J. Am. Chem. Soc. **103**, 241–243 (1981).
[67]Y. Otsuki, S. Kimura, S. Awaji, and M. Nakano, "Magnetocapacitance effect and magnetostriction by the field-induced spin-crossover in [Mn^{III}(taa)]," AIP Adv. **9**, 085219 (2019).
[68]J.-X. Yu, D.-T. Chen, J. Gu, J. Chen, J. Jiang, L. Zhang, Y. Yu, X.-G. Zhang, V. S. Zapf, and H.-P. Cheng, "Three Jahn-Teller states of matter in spin-crossover system Mn(taa)," Phys. Rev. Lett. **124**, 227201 (2020).
[69]J. P. Perdew, K. Burke, and M. Ernzerhof, "Generalized gradient approximation made simple," Phys. Rev. Lett. **77**, 3865–3868 (1996).
[70]G. Kresse and J. Furthmüller, "Efficient iterative schemes for *ab initio* total-energy calculations using a plane-wave basis set," Phys. Rev. B **54**, 11169–11186 (1996).
[71]S. Hill, R. S. Edwards, N. Aliaga-Alcalde, and G. Christou, "Quantum coherence in an exchange-coupled dimer of single-molecule magnets," Science **302**, 1015–1018 (2003).
[72]A. Wilson, S. Hill, R. S. Edwards, N. Aliaga-Alcalde, and G. Christou, "Entanglement of exchange-coupled dimers of single-molecule magnets," AIP Conf. Proc. **850**, 1141–1142 (2006).
[73]R. Tiron, W. Wernsdorfer, D. Foguet-Albiol, N. Aliaga-Alcalde, and G. Christou, "Spin quantum tunneling via entangled states in a dimer of exchange-coupled single-molecule magnets," Phys. Rev. Lett. **91**, 227203 (2003).
[74]T. N. Nguyen, W. Wernsdorfer, K. A. Abboud, and G. Christou, "A supramolecular aggregate of four exchange-biased single-molecule magnets," J. Am. Chem. Soc. **133**, 20688–20691 (2011).
[75]T. N. Nguyen, M. Shiddiq, T. Ghosh, K. A. Abboud, S. Hill, and G. Christou, "Covalently linked dimer of Mn_3 single-molecule magnets and retention of its structure and quantum properties in solution," J. Am. Chem. Soc. **137**, 7160–7168 (2015).
[76]V. S. Zapf, D. Zocco, B. R. Hansen, M. Jaime, N. Harrison, C. D. Batista, M. Kenzelmann, C. Niedermayer, A. Lacerda, and A. Paduan-Filho, "Bose-Einstein condensation of $S = 1$ nickel spin degrees of freedom in $NiCl_2 - 4SC(NH_2)_2$," Phys. Rev. Lett. **96**, 077204 (2006).
[77]S. A. Zvyagin, J. Wosnitza, C. D. Batista, M. Tsukamoto, N. Kawashima, J. Krzystek, V. S. Zapf, M. Jaime, N. F. Oliveira, and A. Paduan-Filho, "Magnetic excitations in the spin-1 anisotropic Heisenberg antiferromagnetic chain system $NiCl_2 - 4SC(NH_2)_2$," Phys. Rev. Lett. **98**, 047205 (2007).
[78]V. S. Zapf, P. Sengupta, C. D. Batista, F. Nasreen, F. Wolff-Fabris, and A. Paduan-Filho, "Magnetoelectric effects in an organometallic quantum magnet," Phys. Rev. B **83**, 140405 (2011).
[79]V. S. Zapf, V. F. Correa, P. Sengupta, C. D. Batista, M. Tsukamoto, N. Kawashima, P. Egan, C. Pantea, A. Migliori, J. B. Betts, M. Jaime, and A. Paduan-Filho, "Direct measurement of spin correlations using magnetostriction," Phys. Rev. B **77**, 020404 (2008).
[80]M. Yazback, J.-X. Yu, S. Liu, L. Zhang, N. S. Sullivan, and H.-P. Cheng, "First-principles study of an $S = 1$ quasi one-dimensional quantum molecular magnetic material," Phys. Rev. B **103**, 054434 (2021).
[81]R. Yu, L. Yin, N. S. Sullivan, J. S. Xia, C. Huan, A. Paduan-Filho, N. F. Oliveira, Jr., S. Haas, A. Steppke, C. F. Miclea, F. Weickert, R. Movshovich, E.-D. Mun, B. L. Scott, V. S. Zapf, and T. Roscilde, "Bose glass and Mott glass of quasiparticles in a doped quantum magnet," Nature **489**, 379 (2012).
[82]A. I. Johnson, F. Islam, C. M. Canali, and M. R. Pederson, "A multiferroic molecular magnetic qubit," J. Chem. Phys. **151**, 174105 (2019).
[83]M. Gakiya-Teruya, X. Jiang, D. Le, Ö. Üngör, A. J. Durrani, J. J. Koptur-Palenchar, J. Jiang, T. Jiang, M. W. Meisel, H.-P. Cheng, X.-G. Zhang, X.-X. Zhang, T. S. Rahman, A. F. Hebard, and M. Shatruk, "Asymmetric design of spin crossover complexes to increase the volatility for surface deposition," J. Am. Chem. Soc. **143**, 14563–14572 (2021).
[84]D. Le, T. Jiang, M. Gakiya-Teruya, M. Shatruk, and T. S. Rahman, "On stabilizing spin crossover molecule $[Fe(tBu_2qsal)_2]$ on suitable supports: Insights from *ab initio* studies," J. Phys.: Condens. Matter **33**, 385201 (2021).
[85]D. Vanderbilt, "Soft self-consistent pseudopotentials in a generalized eigenvalue formalism," Phys. Rev. B **41**, 7892–7895 (1990).
[86]G. Kresse and D. Joubert, "From ultrasoft pseudopotentials to the projector augmented-wave method," Phys. Rev. B **59**, 1758–1775 (1999).

[87]C. G. Broyden, "A class of methods for solving nonlinear simultaneous equations," Math. Commun. **19**, 577–593 (1965).
[88]H.-r. Fang and Y. Saad, "Two classes of multisecant methods for nonlinear acceleration," Numer. Linear Algebra Appl. **16**, 197–221 (2009).
[89]CUDA toolkit documentation, https://docs.nvidia.com/cuda/index.html, 2021, version: v11.2.1.
[90]N. M. Josuttis, *The C++ Standard Library: A Tutorial and Reference*, 3rd ed. (Addison-Wesley, Philadelphia, PA, 2000).
[91]NVCC compiler, https://docs.nvidia.com/cuda/cuda-compiler-driver-nvcc/, 2021.
[92]A. Kozhevnikov, M. Taillefumier, S. Pintarelli, I. Sivkov, and T. C. Schulthess (2021). "The SIRIUS library," GitHub. https://github.com/electronic-structure/SIRIUS.